RSC Advances

PAPER

View Article Online
View Journal | View Issue

Cite this: *RSC Adv.*, 2026, **16**, 13597

Interfaced FeS/g-C_3N_4 hybrid material for charge transport in supercapacitors

Sohail Ahmad,[a] Hao Zhang,*[b] Sijie Zhang,*[cd] Areej Fatima,[e] Ibad Alam,[e] Abdus Sami,[f] Ayman A. Aly,[g] Alsharef Mohammad,[h] Mohammed M. Fadhali[i] and Abdullah H. Alshahri[j]

Transition metal sulfides offer multiple favorable properties as electrode materials in supercapacitors owing to their diverse redox chemistry, high theoretical capacitance, and different topologies. They exhibit better electrochemical properties when paired with carbon materials. The effective fabrication of a FeS/g-C_3N_4 nanocomposite, in which the FeS nanoparticles are evenly adhered to a conductive g-C_3N_4 framework, was accomplished in this study. The hybrid system improves charge transfer and structural stability by combining the pseudocapacitive properties of FeS with the large area, layered structure, and conductivity of g-C_3N_4. The g-C_3N_4 matrix has a high capacity to inhibit the agglomeration of FeS nanoparticles, boost the exposure of electroactive groups, and facilitate rapid ion/electron movements. Consequently, the FeS/g-C_3N_4 electrode outperforms the immaculate FeS with a high specific capacitance (C_{sp}) of 802.5 F g^{-1} at 1 A g^{-1} and 475 F g^{-1} at 5 A g^{-1}. Further long-term cycling studies reveal the outstanding stability of the electrode with 72.34% capacitance retention despite 5000 cycles. Besides, the composite exhibits exceptional energy and power densities, with an efficient energy density (E_D) of 17.83 Wh kg^{-1} at a power density (P_D) of 200 W kg^{-1} and 10.56 Wh kg^{-1} at 1.0 kW kg^{-1}. This excellent electrochemical performance is owing to the synergistic effect of FeS and g-C_3N_4, which increases redox activity, enhances charge transfer and minimizes internal resistance. Our findings show that FeS/g-C_3N_4 might serve as a feasible option for long-term, high-performance supercapacitor electrodes in next-generation energy storage applications.

Received 6th December 2025
Accepted 16th February 2026

DOI: 10.1039/d5ra09426g

rsc.li/rsc-advances

1. Introduction

Improved energy storage systems are urgently needed to address several global issues, including the depletion of fossil fuel sources, the increasing consequences of global warming, and the rising energy consumption in various sectors.[1–3] In response to such needs, there is a significant demand on energy storage technologies, which should not only be efficient and high-performing but also economically feasible, sustainable, and ecologically benign.[4–6] There has been extensive research on the development of clean and renewable sources of energy over the previous few years. Despite the potential of renewable sources, their scarcity makes it difficult to meet the growing demand for energy.[7–9]

To overcome these issues, research on electrochemical energy storage (EES) devices has advanced significantly as a potential replacement for traditional fossil-based systems.[10–12] Among EES technologies, supercapacitors (SCs) have drawn a lot of attention because of their low-cost structure, quick charge/discharge profiles, and high P_D.[13] SCs are generally categorized into three major categories based on their charge storage: electric double-layer capacitors (EDLCs), pseudo capacitors (PCs), as well as hybrid supercapacitors (HSCs).[14–16] PCs store charge *via* faradaic redox reactions occurring on the surface or near the surface of active materials, which include conductive polymers, hydroxides, sulfides and transition metal oxides. Although PCs may attain a much higher capacitance than EDLCs, structural features can cause PC performance to deteriorate with time.[17–20]

[a]*School of Mechanical Engineering, Guizhou University of Engineering Science, Guizhou, 551700, P. R. China*

[b]*School of Chemical Engineering, Guizhou University of Engineering Science, Bijie 551700, P. R. China. E-mail: zhanghao4921@126.com*

[c]*School of Science, Guizhou University of Engineering Science, Bijie 551700, China. E-mail: sijie.zhang@scu.edu.cn*

[d]*College of Physics, Sichuan University, Chengdu 610065, China*

[e]*Institute of Chemical Sciences, Bahauddin Zakariya University, Multan, 60800, Pakistan*

[f]*Centre of Excellence in Solid State Physics, University of the Punjab (PU), 54000, Lahore, Pakistan*

[g]*Department of Mechanical Engineering, College of Engineering, Taif University, Taif 21944, Saudi Arabia*

[h]*Department of Electrical Engineering, College of Engineering, Taif University, Taif 21944, Saudi Arabia*

[i]*Department of Physical Sciences, Physics Division, College of Science, Jazan University, P.O. Box. 114, Jazan 45142, Kingdom of Saudi Arabia*

[j]*Department of Civil Engineering, College of Engineering, Taif University, P.O. Box 11099, Taif City 21974, Saudi Arabia*

The ideal way to bridge the gap between high power and high energy storage with the beneficial synergistic properties of complementary materials is by using hybrid supercapacitors (HSCs), which combine the qualities of both EDLCs and PCs.[21–24] Due to their high theoretical capacitance and diverse redox chemistry, transition metal chalcogenides (TMCs), such as oxides, sulfides, selenides, and tellurides, have gained popularity recently.[25–27] Among them, it is possible to identify materials such as iron sulfide (FeS), which, in addition to its low price, natural abundance, environmental friendliness, and ease of synthesis, boasts a range of qualities. However, the full potential of FeS as a high-performance electrode material is hampered by problems such as minimal intrinsic conductivity, poor ion diffusion profile, and high-rate charge/discharge capacity restrictions.[28,29]

Solutions to these challenges involve creating FeS-based nanocomposites with modified morphologies, including nanosheets, nanorods, and nanoflowers, and combining them with conductive scaffolds, like reduced graphene oxide (rGO), alongside graphitic carbon nitride (g-C_3N_4).[30,31] One such supporting material, g-C_3N_4, has been widely utilized because of its appropriate bandgap, strong chemical stability, planar layered structure, affordability, and accessibility of raw materials. The integration of g-C_3N_4 into composite systems has been shown to improve the surface area and electroactive material transport, providing a robust support network to electroactive materials.[32–34]

A NiS-g-C_3N_4 hybrid, created by Mukhtiar Hussain *et al.*, demonstrated an impressive current density of 933.78 F g^{-1} (C_{sp}) at 1 A g^{-1}, shedding light on the potential structural and electrochemical enhancements of g-C_3N_4. Additionally, it was found to maintain active sulfide materials during repeated charge–discharge cycles, as evidenced by a high coulombic efficiency of 92.80%, outstanding stability throughout cyclic cycles, and retention of 97% capacitance after 5000 cycles.[35] Based on this, Thirumoorthy Kulandaivel *et al.* studied a g-C_3N_4/sulfur@MnS composite. They found that adding sulfur and manganese sulfide to g-C_3N_4 improved electron and ion transport, resulting in a C_{sp} of 493 F g^{-1} at 0.5 A g^{-1}. The hybrid device constructed using this composite and activated carbon demonstrated the capacity of g-C_3N_4 to improve the energy delivery of the full-cell and its operational stability by producing an E_D of 18.7 Wh kg^{-1} and maintaining capacitance of 81% after 5000 cycles.[36] Building on this design technique, S. Maruthasalamoorthy *et al.* placed La-doped Bi_2S_3 into the g-C_3N_4 (ref. 37) matrix, obtaining a high electrochemical capacity of 1880 C g^{-1}. This enhancement was largely explained by the larger surface area (131.4 m^2 g^{-1}) and the existence of a significant number of redox-active sites *via* the synergistic effect of La doping and g-C_3N_4 support. Even with a comparatively low 1.7 Wh kg^{-1} E_D and 64% retention after 10 000 cycles, the system continued to function successfully when stacked in an imbalanced system with rGO. These are continual advancements in the sulfide g-C_3N_4 composites, revealing the major function of the material in accelerating the flow of electrons, improving mechanical stability, and dispersing electroactive materials. Still, even with these encouraging findings, FeS-based systems coupled with g-C_3N_4 remain under-investigated, which is noteworthy considering the nature of FeS with the redox activity, natural occurrence, and environmental friendliness. The presence of this gap presents an opportune and fascinating prospect of researching FeS/g-C_3N_4 hybrids as the next generation of supercapacitor materials that have a capability to bring together high capacity, stability, and cost-effectiveness in a single line.

In this work, we prepared a FeS/g-C_3N_4 hybrid nanocomposite using a hydrothermal procedure and evaluated its potential as an electrode for supercapacitor applications. The subsequent FeS/g-C_3N_4 combination resulted in a dramatic improvement in electrochemical performance. Specifically, FeS/g-C_3N_4 demonstrated a high-rate capability and a high C_{sp} of 802.5 F g^{-1} at 1 A g^{-1} and 475 F g^{-1} at 5 A g^{-1}. This enhancement is ascribed to the large number of redox-active sites offered by both FeS and g-C_3N_4 because of the synergistic interaction that results in the fast movement of electrons and ions and limits structural degradation further during the cycling process. These results make FeS/g-C_3N_4 composite a very promising material for applications in the future generation energy storage devices.

2. Experimental analysis

2.1 Materials and reagents

This investigation used analytical-quality substances and unpurified chemicals. Thiourea (≥99%, Sigma-Aldrich). Sodium hydroxide (NaOH, Merck), thioacetamide (≥99%, Sigma-Aldrich), and iron(II) chloride tetrahydrate ($FeCl_2 \cdot 4H_2O$, ≥99%, Sigma-Aldrich). Deionized (DI) water, ethanol (≥99.8%, Merck), and isopropanol (≥99.5%, Merck). Nitric acid (HNO_3, 0.1 M, Merck). All reagents were analytical grade and did not require further purification. In every experiment, DI water (18.2 MΩ cm, Millipore system) was utilized.

2.2 Fabrication of FeS

For the preparation of FeS through the hydrothermal method, deionized water was deoxygenated with N_2; $FeCl_2 \cdot 4H_2O$ (0.299 g, 1.5 mmol) was dissolved in 30 mL of water, and 1–5 mM ascorbic acid was added to maintain Fe^{2+}; in a different beaker, thioacetamide (C_2H_5NS) (0.225–0.338 g, 3.0–4.5 mmol) was dissolved in 10 mL of water. The above-mentioned two solutions were mixed while stirring, and 1 M NaOH was used to adjust the pH to 7.5–9.0 (PVP K30, 100–300 mg added to control particle growth). Approximately 40 mL of the mixture was added to a 50 mL Teflon-lined autoclave (≤80% fill), sealed, and heated at 160 °C for 8–12 h. After the mixture was naturally cooled to room temperature, the black precipitate was collected by centrifugation and washed twice with water, followed by two washes with ethanol or isopropanol.

2.3 Synthesis of g-C_3N_4

To synthesize graphitic carbon nitride (g-C_3N_4), thiourea was thermally polycondensed. Ten grams of thiourea were first dried for 24 h at 100 °C, then calcined for four hours at 550 °C in a covered silica crucible. To get rid of any remaining alkaline contaminants, the resultant yellow powder was thoroughly cleaned with 0.1 M HNO_3 solution and then with deionized

water. Finally, to obtain pure g-C_3N_4 powder, the product was dried in a hot-air oven for 24 hours at 80 °C.

2.4 Synthesis of FeS/g-C_3N_4

Pre-synthesized FeS nanoparticles and g-C_3N_4 were then combined to synthesize the FeS/g-C_3N_4 nano-hybrid with a weight ratio of FeS to g-C_3N_4 of 1 : 2. Typically, 0.50 grams of FeS and 1.00 grams of g-C_3N_4 were introduced into 100 mL of deoxygenated deionized water. The suspension was then stirred with a magnet for 30 minutes at ambient temperature to facilitate pre-homogenization. The mixture was then subjected to ultrasonication for 20 minutes at 200 W and 40 kHz using a probe sonicator to achieve a homogeneous dispersion of FeS nanoparticles on the g-C_3N_4 substrate. The resultant homogenous solution was filled to a maximum of 80% of its entire volume in a Teflon-lined stainless-steel autoclave that was subjected to a 12-hour hydrothermal treatment at 100 °C. After the product was naturally cooled to room temperature, it was centrifuged at 8000 rpm for 10 minutes to eliminate any remaining contaminants by washing it with ethanol and deionized water. Finally, to create the FeS/g-C_3N_4 compound powder, the crystalline product was dried in a hot-air oven at 80 °C for 5 h (Fig. 1).

2.5 Structural characterizations

The DX-2700BH was used to collect the XRD patterns of all synthesized materials for structural investigation. At 300 mA and 40 kV, the diffractometer utilized a $\lambda = 1.54051$ Å from a Cu-Kα source. XRD data of the synthetic materials were attained in the 2θ range (20°–80°) at a scanning speed of 5° per minute. Using APREO-2C-HIVAC equipment at a rising voltage of 10 kV, SEM and EDS (scanning electron microscopy and energy-dispersive X-ray spectroscopy) were operated to examine the surface characteristics in combination with the elemental composition of the obtained materials. For transmission electron microscopy (TEM), the JEM-F200 instrument under 200 kV was employed. The Micromeritics ASAP 2460 device was used to perform a Brunauer–Emmett–Teller (BET) and Barrett–Joyner–Halenda (BJH) analysis and determine the surface area of the materials. The sample was analyzed under mesoporous conditions, with a degassing temperature of 150 °C for 12 hours. Using the KBr pellet approach, the Bruker VECTOR 22 spectrometer was used for FTIR analysis to assess the mid-infrared region of the synthesized materials (4000–300 cm^{-1}). Raman spectroscopy was conducted using the HORIBA HR Evolution laser confocal Raman system, using a 633 nm excitation wavelength, a power of 1 mW, and a spectral range of 50–4000 cm^{-1}.

2.6 Preparation of the working electrode

Ni foam, cut into small 1 × 1 cm pieces, was used to prepare the working electrode. After that, for ten minutes each, these pieces were successively cleaned with 100% ethanol, 10% HCl, DIW, and acetone. 5.0 mg of the final material was dissolved in 100 µL DIW and sonicated for 15 minutes. Then, the electrode material, active carbon, and PVDF were mixed in a mass ratio of 8 : 1 : 1, and *N*-methylpyrrolidone (NMP) was added and stirred for 4 hours to obtain a homogeneous mixture. The drop-coating procedure was used to prepare the working electrode, where the nickel foam (NF) was coated with the liquid. For 12 hours, the functionalized NF was vacuum-dried at 70 °C. The active mass was about 1.5 mg.

2.7 Electrochemical techniques

The electrochemical capabilities of the prepared electrodes were tested in a three-electrode arrangement using the CHI-760E electrochemical workstation. This design utilized platinum wire, Ag/AgCl, and our synthetic substance as the counter, reference, and working electrodes, respectively. All experiments

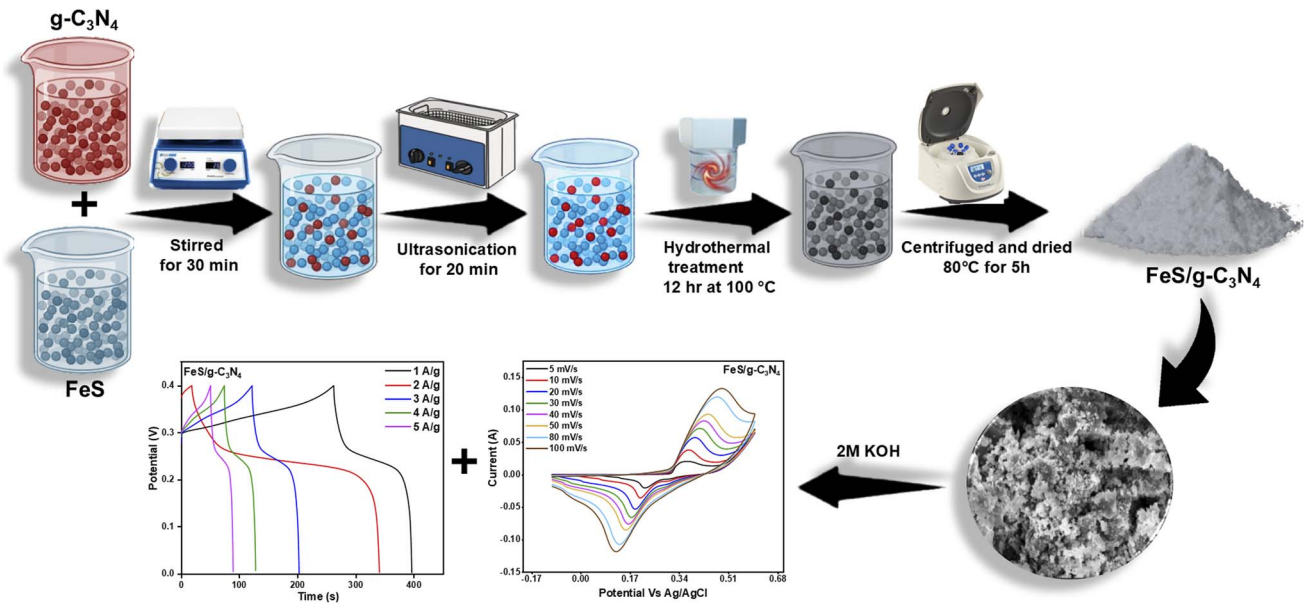

Fig. 1 Schematic of the synthesis of the FeS/g-C_3N_4 nanocomposite.

were done in 2 M KOH. Cyclic voltammetry (CV), an electrochemical technique used to evaluate redox behavior and charge storage properties, was performed at scan rates ranging from 5 to 100 mV s^{-1} within a potential window of −0.2 to 0.7 V (*vs.* Ag/AgCl).[38] C_{sp} values were computed from the CV graph using eqn (1).

$$C_{sp} = \int_{v_c}^{v_a} \frac{I \times dv}{m \times S \times \Delta V} \quad (1)$$

S, I, m, and dv are the scan rate, monitored current, substrate mass, and potential variation. The experiment included galvanostatic charge–discharge (GCD) measurements with current densities (C_D) of 1, 2, 3, 4, and 5 A g^{-1} (C_D). GCD polarization curves from eqn (2)–(4) were used to calculate C_{sp}, power density (P_D), and energy density (E_D) .[39,40]

$$C_{sp} = \frac{I \times \Delta t}{m \times \Delta V} \quad (2)$$

$$E_d = \frac{C_{sp} \times \Delta V^2}{7.2} \quad (3)$$

$$P_d = \frac{E \times 3600}{\Delta t} \quad (4)$$

I, Δt, and m indicate the current, time change, and mass of the conductive substrate. Electrochemical impedance spectroscopy (EIS) was performed at 0.01–20 kHz with a 0.5 V supplied voltage to measure the resistance of the material. Eqn (5) was used to calculate the conductivity of the synthesized nanomaterials.[38]

$$\sigma = \frac{L}{R_{ct} \times A} \quad (5)$$

A is the surface area of the working electrode, L is the electrode distance, and R_{ct} is the EIS. Double-layer capacitance (C_{dl}) of the synthesized electrocatalyst was investigated using CV at different scan speeds, with a focus on the non-faradaic zone.

3. Results and discussion

3.1 Morphological analysis

SEM, EDX, and elemental mapping were used to systematically acquire data on the morphological characteristics and elemental composition of FeS, g-C_3N_4, and FeS/g-C_3N_4 composite, as shown in Fig. 2 and S1. A schematic image of the morphological aspects of FeS, g-C_3N_4, as well as the composite of FeS/g-C_3N_4, is presented in Fig. 2a. The SEM images are presented in Fig. 2(b–d). Pure FeS, as shown in Fig. 2b, with densely stacked, evenly scattered nanograins that have polyhedral forms, are well-crystallized, and do not clump into particles. The image of pure g-C_3N_4 in Fig. 2c features an interconnecting structure that implies a porous network. On the other hand, FeS/g-C_3N_4 (Fig. 2d) shows a plate-like shape, characteristic of graphitic g-C_3N_4, thus corroborating the fact that FeS was trapped within the plate-like structure. Elemental analysis and spatial analysis were conducted using EDX and elemental mapping. Fig. 2e displays the spectra and mappings of the FeS/g-C_3N_4 composite, revealing the presence of Fe, S, C, N, O, and Pt. The signal obtained from the Pt conductor is a consequence of the sputtered conductive Pt coating applied to the sample prior to SEM analysis and does not reflect the intrinsic compositional properties. The detected O signal might be attributable to surface oxidation of FeS, adsorption of ambient oxygen species, or functional groups that are still oxygenated in g-C_3N_4 or introduced during synthesis and washing. Elemental maps establish a homogeneous distribution of Fe, S, C and N, which correlates to close interfacial contact and homogenous mixing between FeS and g-C_3N_4. To assure comparability, EDX spectra and elemental maps of each of the constituents are included in the supplementary material. Fig. S1a depicts the EDX and mapping of pure FeS, where it is obvious that there was a uniform distribution of Fe and S, and consequently purity of the phase. The corresponding results on pristine g-C_3N_4 in Fig. S1b show that C and N are consistently distributed, thus proving its chemical identity and purity. Together, the well-defined morphologies and the homogenous distribution of elements in the FeS/g-C_3N_4 composite are predicted to promote efficient charge transfer and better electrochemical functioning in energy-related applications.

The size, shape, and dispersion of the produced materials may all be precisely analyzed *via* TEM, as shown in Fig. 3. The TEM images of FeS, g-C_3N_4, and FeS/g-C_3N_4 are shown in Fig. 3a–c. FeS nanoparticles have *s* distinct spherical shape and measure 32.63 nm in size. As might be anticipated from a graphitic structure, pristine g-C_3N_4 has a larger, layered morphology with an average size of 69.9 nm. The FeS/g-C_3N_4 composite nanoparticles (28.32 nm) are evenly distributed over the g-C_3N_4 nanosheets, demonstrating the strong interfacial contact and confinement effect. Plots of the particle size distribution are shown in Fig. 3d–f, which validates these average sizes and shows that the nanoparticles are homogeneous. The HRTEM images in Fig. 3g–i provide crystallographic information of materials and demonstrate their crystallinity in the form of distinct lattice fringes. The interplanar distance between the (112) and (203) planes of FeS are 0.252 nm and 0.169 nm, respectively. The lattice spacing of the (002) plane in pristine g-C_3N_4 is 0.323 nm. The lattice spacings of the (102) and (112) planes of the FeS/g-C_3N_4 composite are 0.222 and 0.142 nm, respectively. These measured *d*-spacings, which are quite consistent with the XRD patterns, validate the structural integrity of the materials. The kinetics of charge transfer, which is crucial for electrochemical usage, is improved by the even distribution, reduced particle size, and strong interfacial contact between FeS and g-C_3N_4.

This is further supported by XRD analysis, which is utilized to assess the crystalline structure of the synthesized samples (see Fig. 4a). It was used to evaluate both synthesized materials throughout the 2θ range of 20°–80°. The XRD peaks of FeS that appeared at 23.99°, 33.02°, 35.49°, 40.72°, 49.30°, 53.94°, 57.33°, 62.28°, 63.84°, 69.45°, 71.80°, and 75.40° correspond to the (111), (102), (112), (202), (321), (203), (322), (402), (004), (431), (214), and (521) crystal planes of FeS indexed to the

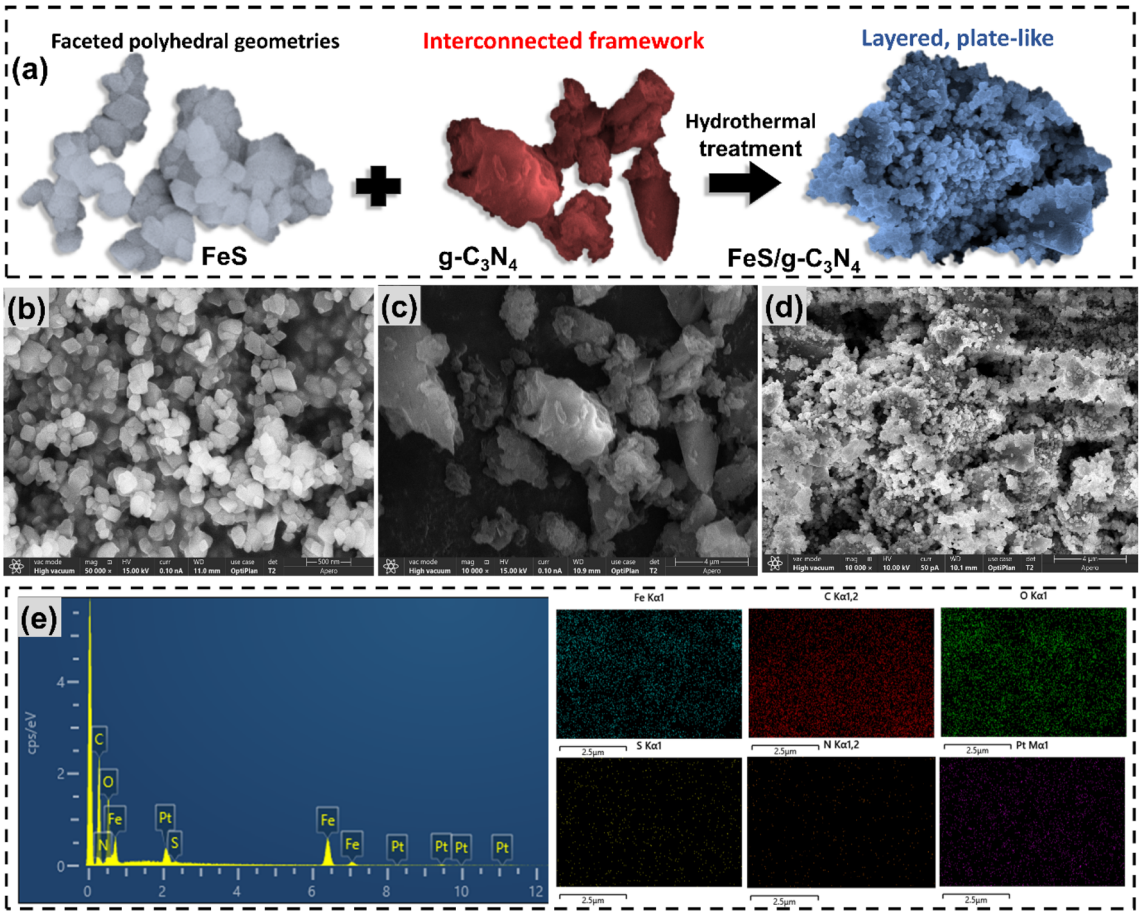

Fig. 2 (a) Schematic representation of morphology of FeS, g-C_3N_4, and FeS/g-C_3N_4; SEM micrographs of (b) FeS, (c) g-C_3N_4, (d) FeS/g-C_3N_4; EDX patterns and the corresponding elemental mappings of (e) FeS/g-C_3N_4.

orthorhombic structure of FeS possessing space group "*Pnma*" and with cell volume 279.95 × 10^6 pm^3 and (JCPDS # 01-076-0963). In the XRD patterns of FeS/g-C_3N_4, all the observed peaks precisely match the FeS peaks, except for one around 26°, and the XRD pattern exhibits a prominent and sharp peak corresponding to the (002) reflection of crystalline graphitic layers in carbon nanotubes.[41] Table 1 presents the extracted XRD parameters, revealing notable structural distinctions between the FeS and FeS/g-C_3N_4 material. Indeed, the composite exhibited a slight shift in the FeS diffraction peaks, indicating lattice strain resulting from strong interfacial contacts between FeS and g-C_3N_4. Such strain can be induced by local bond distortions (such as Fe–N or S–C) and electronic coupling, which slightly alter the FeS lattice characteristics. These structural modifications confirm intimate interactions at the heterojunction. Fig. 4a shows the structural differences between pure FeS and the FeS/g-C_3N_4 composite. The crystallite size (D) is calculated using the Debye–Scherrer's formula.[42,43]

$$D = \frac{K \times \lambda}{\beta \times \cos\theta} \quad (6)$$

Here, $\lambda = 0.15418$ nm, $K = 0.9$ is the shape factor, β is the full-width at half maxima, and θ is the diffraction angle. The pristine FeS sample exhibited a smaller D of 50.20 nm compared to the FeS/g-C_3N_4 composite of 54.59 nm, suggesting a decrease in lattice disorder and particle agglomeration during the composite preparation. This expansion may influence surface-active sites and interface charge flow, suggesting a slight decrease in structural dispersity. Furthermore, structural XRD parameters, such as lattice strain (LS), dislocation density (δ), microstrain (ε), and crystallinity, can be calculated using eqn (7–10).[44,45]

$$\delta = \frac{1}{D^2} \quad (7)$$

$$\varepsilon = \frac{\beta\cos\theta}{4} \quad (8)$$

$$\mathrm{LS} = \frac{\beta}{4\tan\theta} \quad (9)$$

$$\text{Crystallinity} = \frac{\text{area of crystalline peaks}}{\text{total area}} \times 100 \quad (10)$$

Consequently, the δ decreased in the composite (3.76×10^{-4} nm^{-2}) relative to pristine FeS (7.71×10^{-4} nm^{-2}), indicating a lower density of defects. Compared to pristine FeS, the ε and LS also exhibited a noticeable reduction in the composite, from

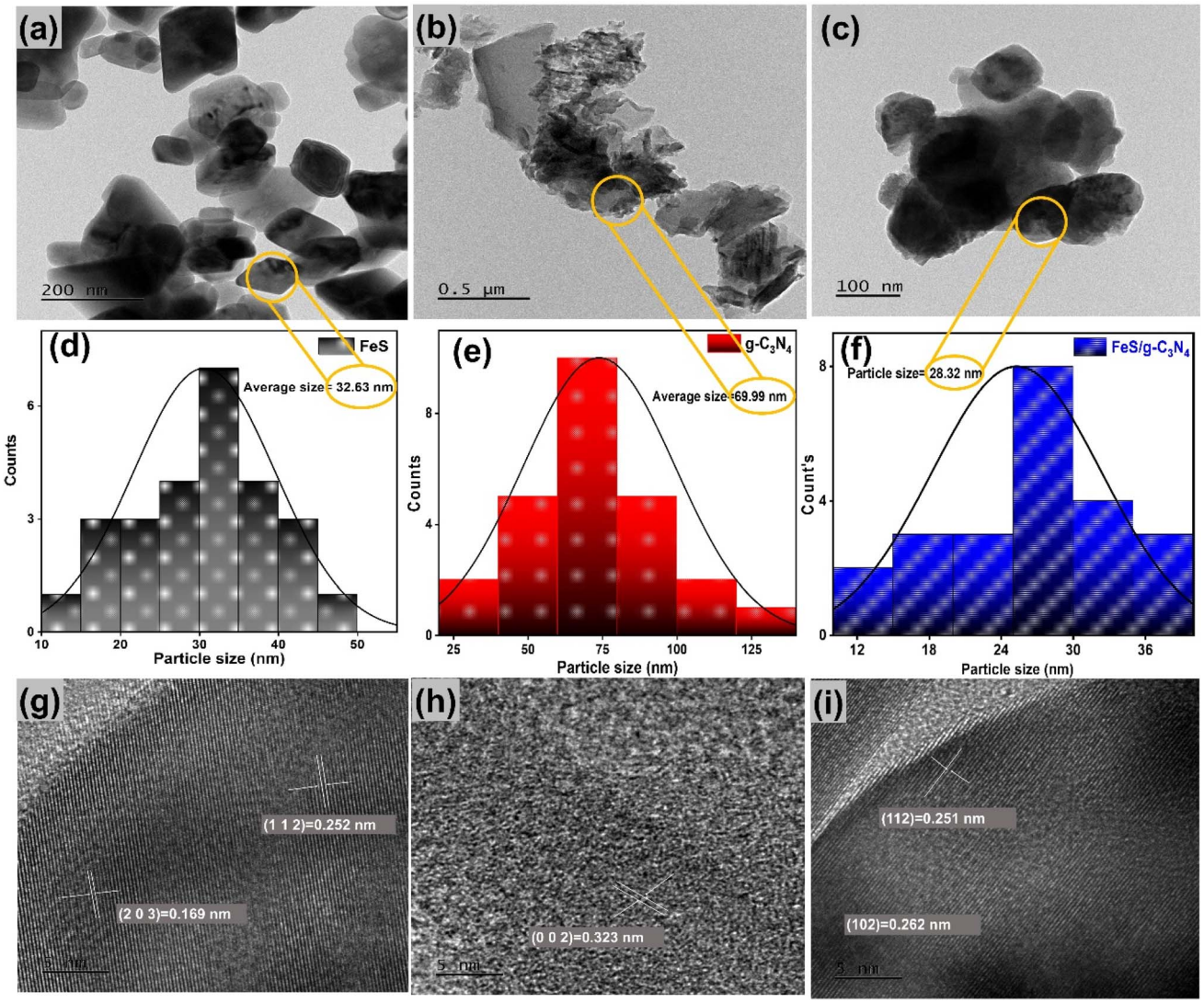

Fig. 3 TEM images of (a) FeS, (b) g-C_3N_4, (c) FeS/g-C_3N_4; average particle size of (d) FeS, (e) g-C_3N_4, and (f) FeS/g-C_3N_4; and HRTEM images of (g) FeS, (h) g-C_3N_4, and (i) FeS/g-C_3N_4.

8.73×10^{-4} to 6.90×10^{-4} and from 2.19×10^{-3} to 1.91×10^{-3}, respectively, indicating minimized lattice distortion due to the interfacial synergy. Furthermore, the crystallinity of pristine FeS (87.03%) surpassed that of the composite (72.37%), which can be attributed to the presence of the amorphous or semi-crystalline g-C_3N_4 phase that disrupts long-range order in the FeS matrix.[46] These variations collectively imply that g-C_3N_4 incorporation not only alters the crystallographic parameters but also introduces structural defects. Additionally, utilizing the crystallographic data from XRD analysis, 3D structural models of FeS were generated. The orthorhombic *Pnma* space group is where FeS crystallizes, as shown by the simulated crystal structure produced using the Diamond program in Fig. 4b. The preferential occupancy of S and Fe atoms at their respective lattice positions is evident from the image. Furthermore, the polyhedral representation of the FeS structure (see Fig. 4c) offers more details on its coordination geometry and structural stability.

The FTIR spectra of the prepared materials are shown in Fig. 4d to verify the successful synthesis of FeS and FeS/g-C_3N_4 composites. The combined FTIR study of FeS, g-C_3N_4, and their composite provides unambiguous evidence of the successful creation of a heterostructure through the preservation and overlap of essential vibrational characteristics. In FeS, the Fe–S stretching vibration observed at 600–800 cm^{-1} indicates the presence of metal–sulfur bonds, while weak peaks around 1600–1650 cm^{-1} (ref. 40) and 3200–3550 cm^{-1} indicate modest surface-bound organic molecules and moisture.[47] For g-C_3N_4, distinctive peaks such as C–H bending at 790–830 cm^{-1}, O–H bending at 1395–1440 cm^{-1}, C=O stretching at 1640–1690 cm^{-1}, along with a broad peak corresponding to O–H stretching at 3300–3400 cm^{-1}, reveal its layered graphitic structure with a polar surface.[48] In the FeS/g-C_3N_4 composite, the C–N stretching at 1640–1690 cm^{-1} is indicative of the g-C_3N_4 backbone, and the spectrum encompasses all crucial features: Fe–S stretching, minor vibrations of C–H[49] and C–N[50] bending

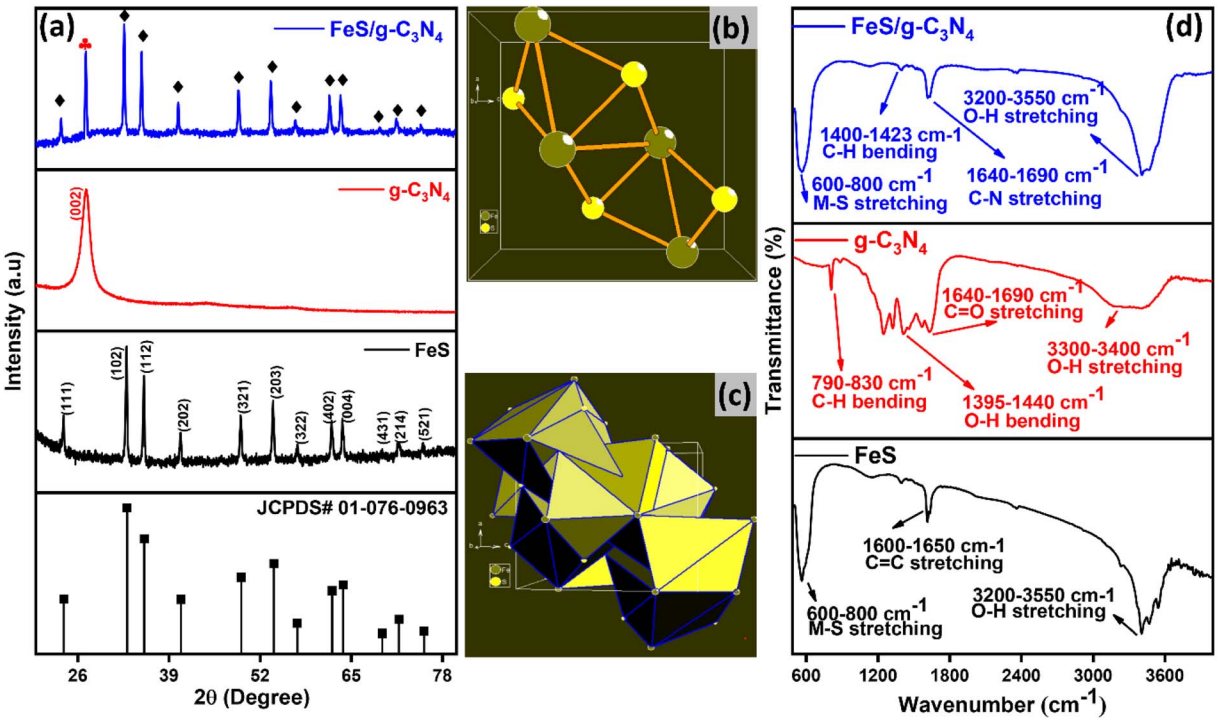

Fig. 4 (a) XRD patterns, (b) 3D structure, (c) polyhedral view of FeS, (d) FT-IR spectra of FeS, g-C_3N_4, and the FeS/g-C_3N_4 nanocomposite.

Table 1 Structural parameters of FeS/g-C_3N_4 and FeS

Material name	D (nm)	$\delta \times 10^{-4}$ (nm^{-2})	$\varepsilon \times 10^{-4}$	LS $\times 10^{-3}$	Crystallinity (%)
FeS	50.20	7.71	8.73	2.19	87.03
FeS/g-C_3N_4	54.59	3.76	6.90	1.91	72.37

and broad O–H stretching, showing that both phases coexist without substantial chemical changes or degradation. This demonstrates that the FeS particles are well integrated into the g-C_3N_4 surface. Additionally, the absence of new peaks or substantial shifts suggests that there is no strong covalent bonding, thereby preserving the intrinsic functions of both materials.

As shown in Fig. 5a, a qualitative investigation using Raman spectroscopy reveals noticeable peaks at approximately 203 and 271 cm^{-1}. The peak at 203 cm^{-1} corresponds to Fe–S asymmetric stretching vibrations and a symmetric Fe–S stretching vibration at 271 cm^{-1}.[51] The FeS/g-C_3N_4 composite exhibits distinctive D and G bands at approximately 1329 and 1596 cm^{-1}, respectively. The *K*-point of the Brillouin zone's phonons and disordered carbon are linked to the D band, which denotes edge states or structural flaws. The E_{2g} stretching vibrations of sp^2-hybridized graphitic domains, which are characteristic of the g-C_3N_4 frameworks, correlate to the G band. Increased electrochemical activity is made possible by moderate graphitization with a significant number of defect sites, as indicated by the intensity ratio (I_D/I_G) of approximately 0.99. Moreover, the crystalline character of FeS in the g-C_3N_4 matrix is confirmed by a Raman signal presented in pristine FeS.[52]

BET surface area analysis (Fig. 5b) and BJH pore size distribution (see Fig. 5c) were used to examine the textural properties of the synthesized materials. The comparatively small surface area of pure FeS was 8.22 m^2 g^{-1}, attributable to its dense morphology and agglomeration, which limit the number of accessible active sites. In contrast, pristine g-C_3N_4 possessed a moderately higher surface area (9.66 m^2 g^{-1}), arising from its layered, porous framework. Remarkably, the FeS/g-C_3N_4 composite displayed a significantly enhanced surface area of 17.57 m^2 g^{-1}, indicating effective anchoring of FeS nanoparticles on the g-C_3N_4 matrix. This hybridization prevents particle aggregation, introduces additional electroactive sites, and enhances interfacial contact, which are favorable for charge storage and ion exchange. The BJH analysis confirmed a mesoporous nature in all samples, with the composite demonstrating the most advantageous porosity parameters, an average pore diameter of 24.13 nm and a pore volume of 0.070 cm^3 g^{-1}—far exceeding those of FeS (9.62 nm, 0.007 cm^3 g^{-1}) and g-C_3N_4 (13.19 nm, 0.020 cm^3 g^{-1}). The enlarged pores and interconnected framework facilitate rapid electrolyte penetration and efficient ion transport, thereby minimizing diffusion resistance. These synergistic enhancements in surface area and porosity directly contribute to the superior electrochemical properties of the FeS/g-C_3N_4 composite, underscoring its potential as an excellent electrode material for supercapacitors and rechargeable batteries.

3.2 Electrochemical properties

The electrochemical characteristics of FeS and FeS/g-C_3N_4 nanocomposite electrodes, including GCD, EIS and CV, were

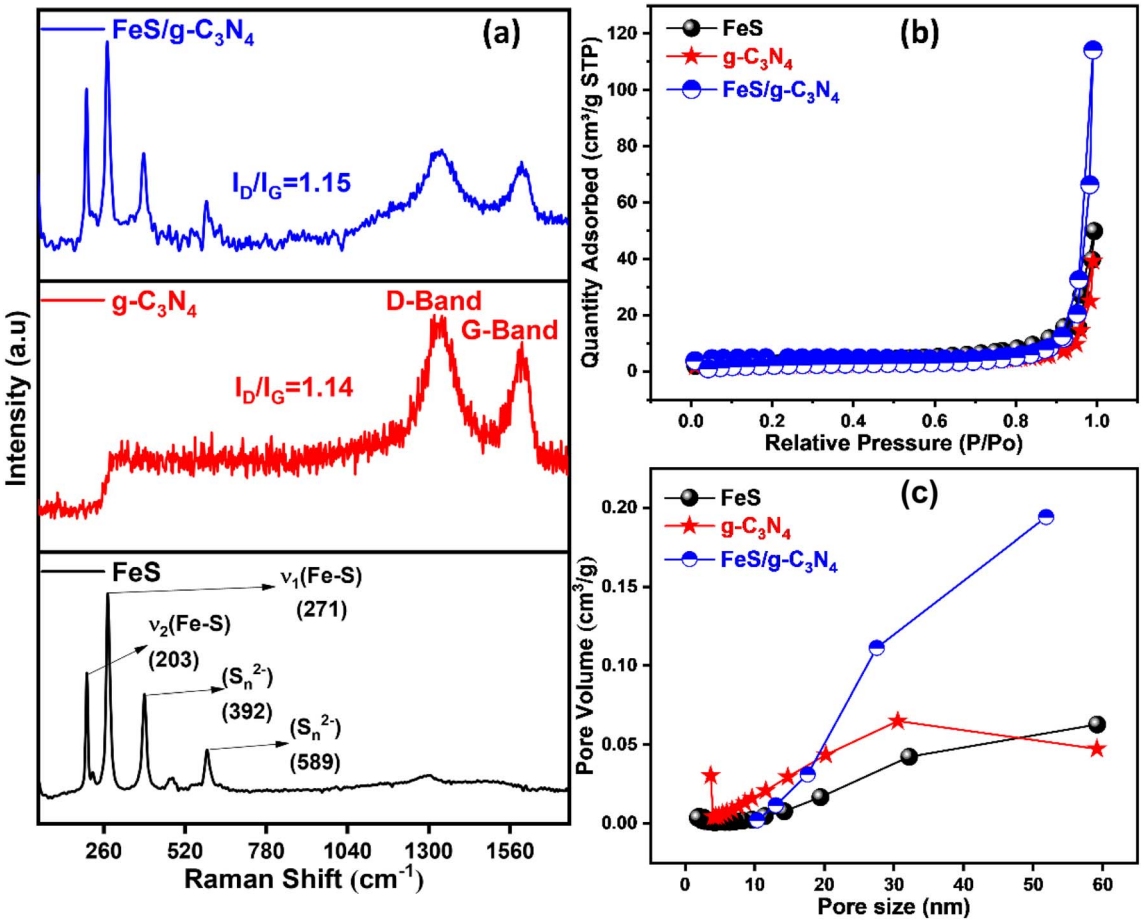

Fig. 5 (a) Raman spectra, (b) BET analysis, and (c) BJH curves of FeS, g-C_3N_4, and FeS/g-C_3N_4 nanocomposite.

methodically examined. The occurrence of distinct redox peaks at the −0.2 + 0.7 V (*vs.* Ag/AgCl) potential window in Fig. 6(a and b) of FeS/g-C_3N_4 and FeS, respectively, indicates that both electrodes possess pseudocapacitive characteristics. The FeS/g-C_3N_4 nanocomposite displayed a significantly larger CV curve area than pure FeS at all scan rates (5–100 mV s^{-1}), suggesting improved charge storage capability and superior electrochemical performance. Since it promotes fast electron transport and inhibits FeS aggregation, this increase is linked to the conductive and layered structure of g-C_3N_4. The redox peaks showed minimal change as the scan rate increased, confirming the excellent electrochemical reversibility. Furthermore, as shown in Fig. 6c and d, the C_p of FeS/g-C_3N_4 was much larger than that of FeS at all scan rates, reaching a maximum of 565.23 F g^{-1} at a scan rate of 5 mV s^{-1}, as opposed to 414.95 F g^{-1} of FeS. As the redox reactions are governed by ion diffusion, higher scan rates limit electrolyte ion transport, leading to a progressive decrease in C_{sp}. Fig. 6e and f indicated that semi-infinite diffusion regulated the redox reaction, even though it showed linear correlations between the peak current and the square root of scan rate ($\nu^{1/2}$), which were calculated using the Randles–Sevcik equation. The FeS/g-C_3N_4 nanocomposite showed higher oxidation and reduction diffusion coefficients than FeS, supporting the premise that the g-C_3N_4 network may enhance ion transport. The electrochemical response of bare NF in the same KOH electrolyte was also evaluated to improve the clarity of the current collector, as shown in Fig. S1(a–c). The NF itself exhibits a mild pseudocapacitive response that results from reversible Ni^{2+}/Ni^{3+} surface redox interactions in basic solutions since the NF CV curves displayed weak and wide redox features. However, at the same scan speeds, the enclosed CV area of NF was much smaller than those of FeS and FeS/g-C_3N_4 electrodes, demonstrating the low intrinsic capacitance contribution. It was confirmed that NF is primarily a conductive rather than an active charge-storage scaffold because the obtained C_{sp} of NF was relatively low 72 F g^{-1} at 5 mV s^{-1}) and declined sharply with scan rate. Additionally, the peak current/$\nu^{1/2}$ curve of NF (Fig. S1c) showed a linear correlation with a correlation coefficient of (R^2) = 0.97–0.98, suggesting the existence of diffusion-controlled kinetics that are comparable to more prevalent pseudocapacitive electrodes but have a much smaller slope than FeS-based electrodes. This suggests that compared to FeS and FeS/g-C_3N_4, ion transport and electrochemical activity are slower and lower in NF. Overall, these results demonstrate that FeS/g-C_3N_4 significantly enhances the contribution of the active material to charge storage and the enhanced electrochemical performance of the composite electrode, even though NF has no impact on the pseudocapacitance of the electrode. Also, the FeS/

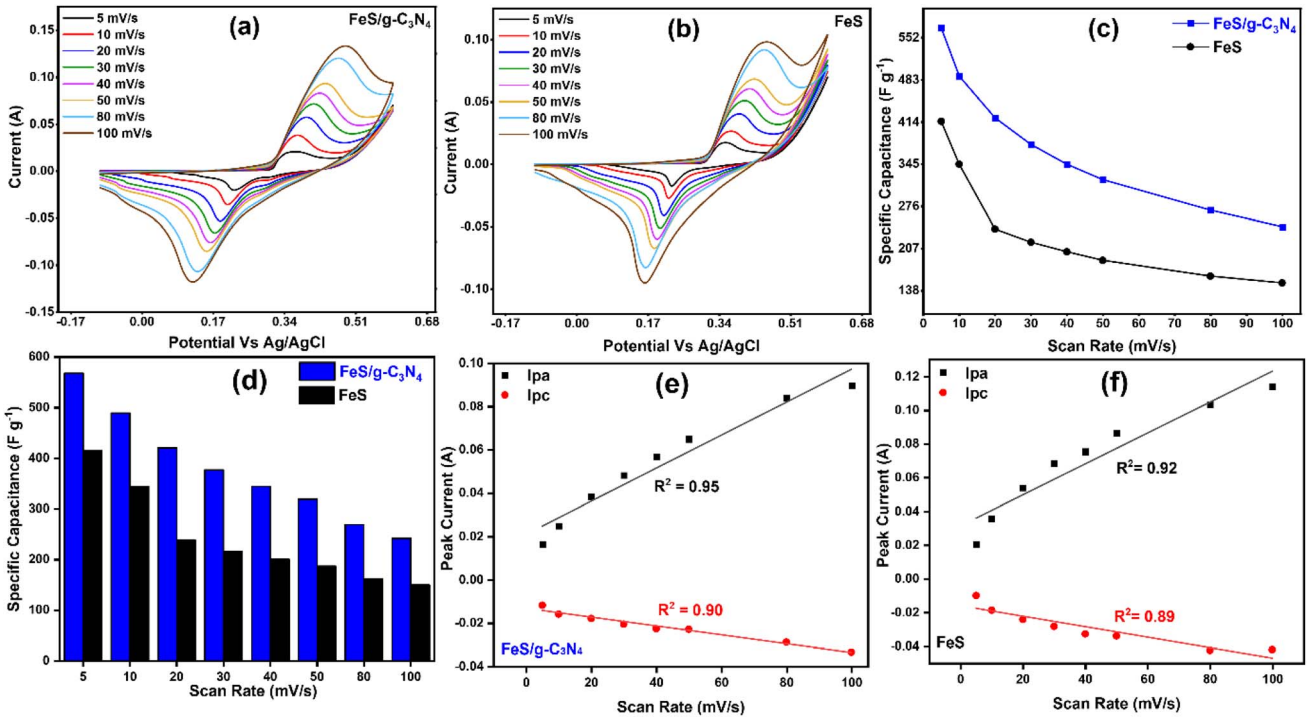

Fig. 6 CV cycles for (a) FeS/g-C_3N_4 and (b) FeS; (c and d) scan rate *versus* specific capacitance plots and scan rate *versus* specific capacitance comparison plot profiles; and (e and f) scan rate *versus* peak current plots for both the materials.

g-C_3N_4 nanocomposite operates as an efficient supercapacitor electrode through a synergistic mechanism, combining pseudocapacitance from FeS and electric double-layer capacitance (EDLC) from g-C_3N_4. FeS undergoes fast and reversible redox reactions involving Fe^{2+}/Fe^{3+} and S^{2-}/S^0 redox couples, primarily represented by eqn (11):[53,54] contributing to high pseudocapacitive charge storage.

$$FeS + OH^- \leftrightarrow FeSOH + e^- \quad (11)$$

However, FeS alone suffers from low conductivity and structural instability. The integration of g-C_3N_4, a nitrogen-rich, conductive 2D material with a large surface area, addresses these issues by acting as a scaffold that conducts electricity and improves electron transport, stabilizes the FeS structure, and provides additional active sites through surface functional groups. This hybrid structure facilitates faster ion/electron mobility, reduces charge-transfer resistance, and enables efficient electrolyte access, resulting in improved C_{sp}, cycle stability and the overall electrochemical performance of the composite.

Fig. 7a and b shows the results of the GCD studies conducted at current densities ranging from 1–5 A g^{-1}, which thoroughly examined the electrochemical properties of pure FeS and FeS/g-C_3N_4 electrodes. The symmetry and linearity of the GCD curves for both electrodes demonstrate strong capacitive reversibility and great coulombic efficiency. However, the synergistic combination of electroactive FeS and the conductive high-surface-area of g-C_3N_4 structure promotes efficient ion diffusion and rapid charge transfer, leading to the much-improved performance of the FeS/g-C_3N_4 complex. The high rate capability of the FeS/g-C_3N_4 electrode is shown by the change in C_{sp} as a function of current density (see Fig. 7c). At 1 A g^{-1}, it has a C_{sp} of 802.5 F g^{-1}, and at 2, 3, 4, and 5 A g^{-1}, it stores 670 F g^{-1}, 615 F g^{-1}, 540 F g^{-1}, and 475 F g^{-1}, respectively. In contrast, the C_{sp} of pure FeS is 377.5 F g^{-1}, which is lower than that of FeS/g-C_3N_4. Fig. S2(a and b) shows that under identical conditions, GCD measurements of bare NF were also performed, which further helps to clarify the function of the current collector. The linear profiles and extremely short discharge durations of NF, GCD curves suggest that their charge storage capabilities are severely lacking. The C_{sp} of NF, which is 5.64 at 1 A g^{-1}, is quite low and rapidly decreases with current density. Reflectively, NF has a maximum E_D of 2.02.5 Wh kg^{-1} at a P_D of around 200 W kg^{-1}. This density decreases with increasing power outputs, but it also increases with a short discharge duration. These results demonstrate that NF is essentially a mechanically robust, conductive current collector that has no effect on the total energy storage of FeS/g-C_3N_4. Based on the C_{sp}, the Ragone plot (Fig. 7d) shows the E_D and P_D. With a high E_D of 17.83 Wh kg^{-1} at a P_D of 200 W kg^{-1} and 10.56 Wh kg^{-1} at a high P_D of 1.0 kW kg^{-1}, the FeS/g-C_3N_4 composite exhibits strong energy storage properties. In contrast, NF has the lowest E_D/P_D in pure FeS, where the E_D (0.19 Wh kg^{-1} at 0.06 W kg^{-1}) decreases more quickly with increasing P_D (Fig. 7e). Overall, the FeS/g-C_3N_4 composite consistently outperforms bare FeS and NF in terms of C_{sp}, E_D, and P_D, demonstrating the significant potential for high-performance and high-power supercapacitor applications. Long-term cycling stability (see Fig. 7f) further validates the

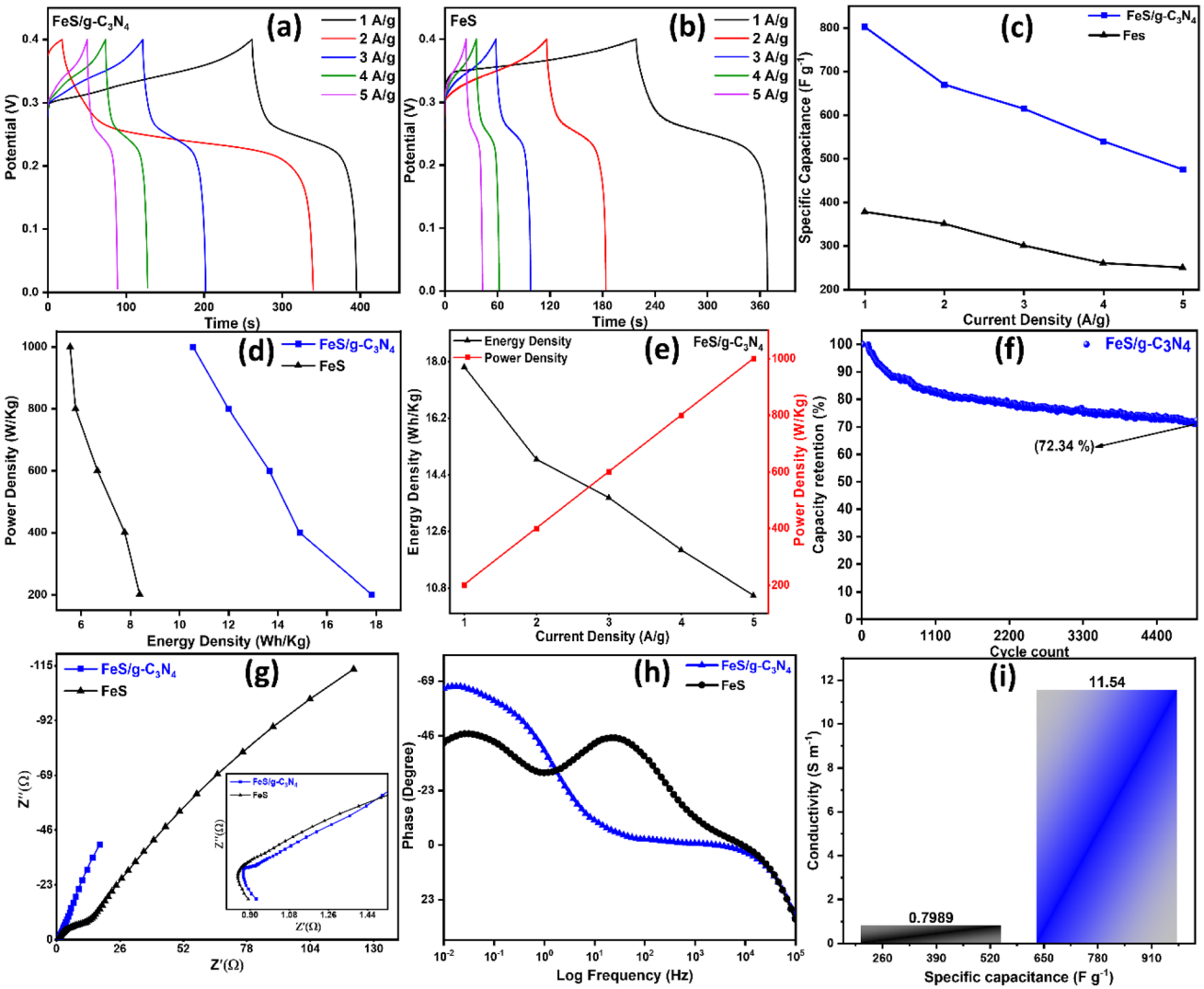

Fig. 7 GCD plots of (a) FeS/g-C_3N_4 and (b) FeS; (c) specific capacitance *versus* current density plots, (d) current density *versus* energy and power density comparison plots of FeS/g-C_3N_4, (e) ragone plots, (f) specific capacitance retention plots, (g) Nyquist plots with an fitted inset plot, (h) bode plots, and (i) specific capacitance and conductivity comparison plots.

robustness of the composite, maintaining 72.34% relative to its initial capacitance on completion of 5000 loops. Collectively, the above findings confirm the incorporation of g-C_3N_4 effectively enhances ion/electron transport, reduces internal resistance, and stabilizes the electrode structure, making FeS/g-C_3N_4 a viable option for high-performance supercapacitors of the future (Table 2).

The charge transport kinetics of FeS/g-C_3N_4 and pristine FeS electrodes were investigated using EIS, as revealed in Fig. 7g–h. The Nyquist plots reveal a smaller semicircle in the high-frequency region for FeS/g-C_3N_4, corresponding to a reduced charge-transfer resistance (R_{ct}) of 1.22 Ω compared to 10.28 Ω for FeS. Likewise, the series resistance (R_s) decreases from 0.86 Ω in pristine FeS to 0.55 Ω in the composite, confirming enhanced electrical contact. The steeper slope in the low-frequency region of FeS/g-C_3N_4 further indicates superior capacitive behavior and faster ion diffusion. The Bode phase analysis supports these observations: FeS/g-C_3N_4 exhibits two distinct relaxation processes associated with interfacial and bulk resistances, while pristine FeS shows less pronounced features, reflecting sluggish electron/ion transport. In addition, the composite achieves a C_{sp} of 802.5 F g^{-1}, nearly double that of pristine FeS (377.5 F g^{-1}), and a markedly higher electrical conductivity (11.54 S cm^{-1} for FeS/g-C_3N_4 *vs.* 0.79 S cm^{-1} for FeS), as shown in Fig. 7i. These findings clearly demonstrate that the conductive and porous g-C_3N_4 framework significantly enhances interfacial contact, accelerates charge transfer, and improves electrolyte accessibility, thereby endowing FeS/g-C_3N_4 with superior energy storage capability compared to bare FeS.

3.3. Asymmetric two-electrode FeS/g-C_3N_4 nanocomposite device

A practical two-electrode asymmetric device was assembled in a standard CR2032 coin cell configuration with FeS/g-C_3N_4 used

Table 2 Comparison of fabricated electrocatalysts with the previously published literature

S. no.	Materials	C_D (A g^{-1})	C_{sp} (F g^{-1})	E_D Wh kg^{-1}	P_D W kg^{-1}	Electrolyte	Ref.
1	C_3N_4/sulfur@MnS	0.5	493	18.7	327	KOH	36
2	g-C_3N_4@SnS_2	0.8	787	56.8	—	KOH	55
3	S-gC_3N_4/CoS_2	1	180 C g^{-1}	32	19.8	KOH	56
4	g-C_3N_4@$CuGaS_2$	1	254	—	—	KOH	57
5	3D-Bi_2S_3@2D-g-C_3N_4	1 mA cm^{-2}	41.53 μAh cm^{-2}	3.17 μWh cm^{-2}	1495 μW cm^{-2}	KOH and PVA gel	58
6	RGO/FeS	1	300	27.91	2093.18	KOH	59
7	Pyrite FeS_2	1	260	46.8	—	Na_2SO_4 and KOH	60
8	FeS/MoS_2	1	991	53	585	KOH	61
9	ZnS/FeS	3	1367.5	—	—	KOH	62
10	2D g-C_3N_4	0.5	137.67	19.33	499.9	H_2SO_4	63
11	MoS_2-g-C_3N_4	1	240.85	—	—	Na_2SO_4	64
12	SnS_2/g-C_3N_4	0.5	552	1.6	3050	KOH	65
13	**FeS/g-C_3N_4**	**1**	**802.5**	**17.83**	**200**	**KOH**	**This study**

on the cathode, activated carbon as the anode, and 3 M KOH electrolyte to evaluate the real-world practical applicability of the synthetic materials (see Fig. 8a). As shown by their electrochemical profiles (see Fig. 8b), FeS/g-C_3N_4 and activated carbon-based electrodes are the best options because they permit a broad working voltage window of 0.0–2.0 V. Even at

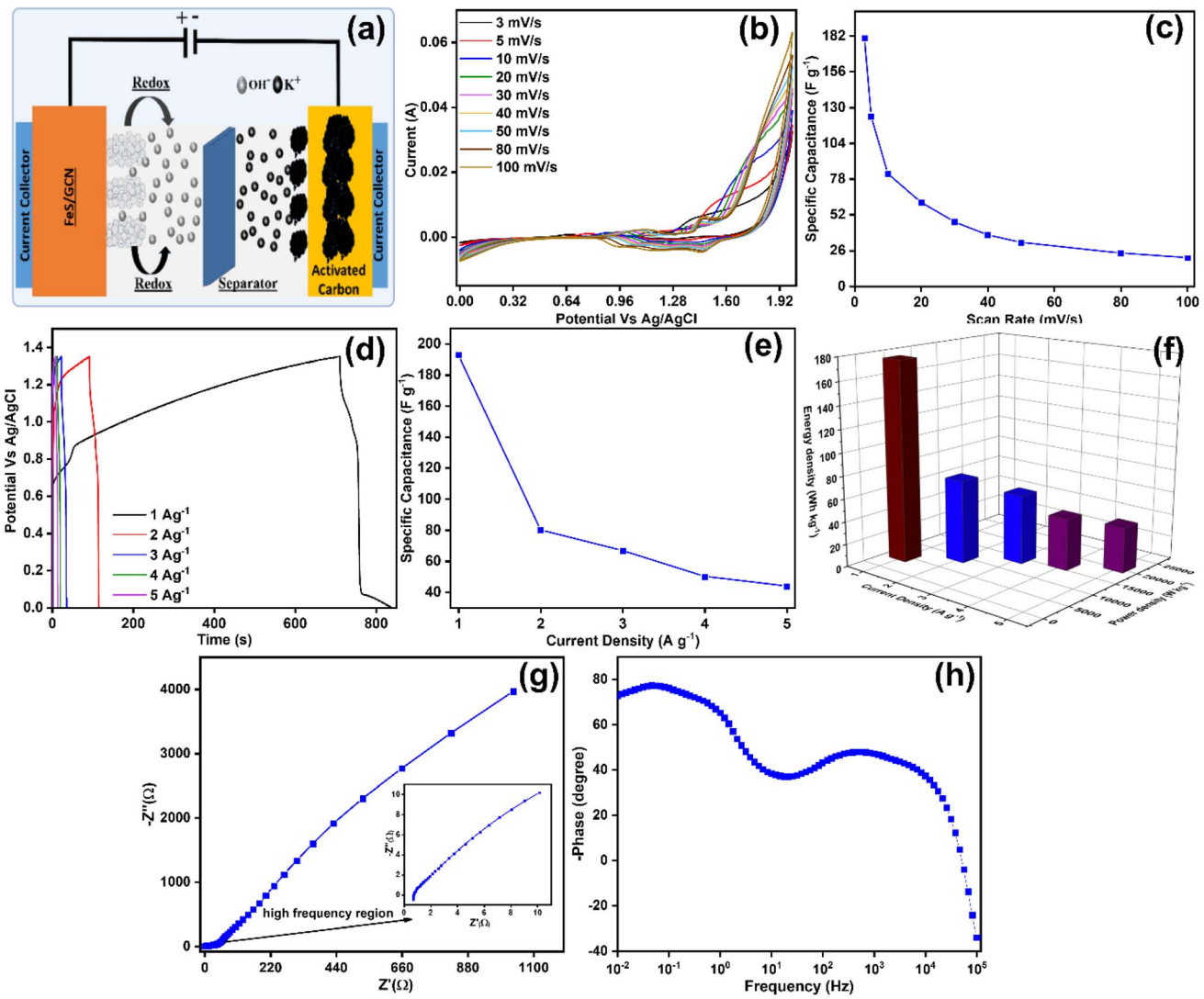

Fig. 8 (a) Schematic of a practical two-electrode device assembled by FeS/g-C_3N_4 nanocomposite, (b) CV curves of practical devices, (c) specific capacitance *versus* scan rate plot, (d) GCD curves, (e) specific capacitance *versus* current density plots, and (f) energy/power density of the device manufactured at different current densities. (g) Nyquist plot of impedance data with an fitted inset plot and (h) bode plot.

scan rates of up to 100 mV s^{-1}, the almost constant form of the CV curves at different scan rates indicates excellent rate capability and negligible polarization. Due to restricted ion diffusion at increasing scan rates, the high C_{sp} of 180.22 F g^{-1} of the device at 3 mV s^{-1} progressively drops to 20.59 F g^{-1} at 100 mV s^{-1} (see Fig. 8c). Superior capacitive reversibility efficiency is confirmed by the symmetric, quasi-triangular shape of GCD curves recorded over the CDs from 1 to 5 A g^{-1} (see Fig. 8d). With a maximum C_{sp} of 192.53 F g^{-1} at 1 A g^{-1}, and 43.75 F g^{-1} retained at 5 A g^{-1} (Fig. 8e), the charge storage performance remains resilient under high-rate conditions. Notably, the device achieves an exceptional E_D of 175.5 Wh kg^{-1} at a Pd of 4.86 kW kg^{-1} and maintains 39.86 Wh kg^{-1} even at an ultra-high P_D of 20.5 kW kg^{-1} (see Fig. 8f). This demonstrates the huge potential of the FeS/g-C_3N_4-based technology for future high-performance energy storage applications.

The following formulae were used to calculate C_{sp}, E_D, and P_D from GCD profiles:

$$C_{sp} = 2 \times \frac{I \times t_d}{\Delta V \times m} \quad (12)$$

$$E_D = \frac{C_{sp} \times (\Delta V)^2}{2} \quad (13)$$

$$P_D = \frac{3600 \times E_D}{t_d} \quad (14)$$

Additionally, as shown in the related EIS plot (see Fig. 8g), it maintains a slight voltage drop. To ascertain the charge transfer kinetics between the electrolyte and the electrode material, the equivalent circuit model was employed. Fig. 8g shows that the R_s value at the real axis intercept was 0.69 Ω. The polarization resistance (R_p) was 59.5 Ω, determined in the high-frequency range using the semicircle diameter. Additionally, two phase shifts are visible in the Bode phase plot, confirming the existence of multiple interfacial charge-transport resistances. Capacitive dominance with little phase lag is indicated by the phase angle being near 90° (see Fig. 8h). These results validate the improved energy-power balance and electrochemical stability provided by the FeS/g-C_3N_4 hybrid design for aqueous supercapacitors.

4. Conclusion

Fabricating a FeS/g-C_3N_4 nanocomposite, in which FeS nanoparticles are uniformly adhered onto a g-C_3N_4 framework, a potential method for creating high-performance supercapacitors is presented in this study. A hydrothermal-assisted synthesis, followed by controlled thermal treatment, enabled the formation of a composite with well-defined nanostructures and enhanced electrochemical characteristics. In addition to the conductive, physically stable, and porous framework provided by the g-C_3N_4 matrix, the inclusion of FeS results in a significant number of redox-spotted sites and substantial theoretical capacities. This combination design increases the rate capacity and long-term stability by improving structural integrity, responding favourably to volume variations throughout the cyclic process, and distributing electrons and transporting ions rapidly. Together, FeS and g-C_3N_4 exhibit a strong synergistic impact that improves C_{sp} in addition to reversibility and electrochemical stability. The FeS/g-C_3N_4 electrode performs very well, exhibiting high E_D and great cycle stability. The hybrid supercapacitor provided an E_D of 175.5 Wh kg^{-1} at a P_D of 4.86 kW kg^{-1} and maintained 39.86 Wh kg^{-1} at a higher P_D of 20.5 kW kg^{-1} after merging into a practical two-electrode asymmetric system (g-C_3N_4/FeS/g-C_3N_4 concentration) in a 3 M KOH solution. According to these findings, FeS/g-C_3N_4 has the potential to serve as a potent and effective electrode material in future supercapacitors. The pseudocapacitive properties of FeS and the conductive pore structure of g-C_3N_4 provide excellent electrochemical resilience and performance, which reveals insightful information for the logical design of scalable and high-performing hybrid energy storage devices.

Author contributions

Sohail Ahmad: conceptualized the research and wrote the main manuscript. Hao Zhang: conducted the experiments, performed data analysis, and reviewed the manuscript writing. Sijie Zhang: designed and implemented the data collection strategy, performed statistical analyses, and provided critical revisions to the manuscript. Areej Fatima: managed the project logistics, coordinated the data collection process, and contributed to the final manuscript review. Ibad Alam: developed the methodology, curated data, assisted in literature review, developed the theoretical framework, and contributed to the discussion and conclusion sections of the manuscript. Abdus Sami: assisted in literature review, developed the theoretical framework, and contributed to the introduction section of the manuscript. Ayman A. Aly: assisted in literature review, developed the theoretical framework, and contributed to the introduction section of the manuscript. Alsharef Mohammad: contributed to methodology, assisted in literature review, and contributed to the discussion and experimental sections of the manuscript. Abdullah H. Alshahri: assisted with experiment setup and data validation, wrote the methodology section writing, edited the overall manuscript and reviewed the results. Mohammed M Fadhali: assisted with experiment setup and data validation, edited the final manuscript and reviewed the results.

Conflicts of interest

The authors declare that the research presented in this article is original and has not been published elsewhere. All data and findings are the result of the authors' own work, and all necessary ethical guidelines and approvals were followed during the course of the study. The manuscript has been reviewed and approved by all authors, and no conflicts of interest exist in relation to the work presented.

Data availability

All the related data are available from the authors upon request.

Supplementary information (SI) is available. See DOI: https://doi.org/10.1039/d5ra09426g.

Acknowledgements

This work was supported by the Guizhou University of Engineering Science High-level Talent Research Startup Fund (No. YuanKe [2025] No. 01), China, the Guizhou Province Science and Technology Innovation Leading Talent Workstation of Solid Functional Materials (KXJZ[2024]015), the Key Laboratory for Research and Development of New Lithium-ion Battery Materials (2023-28), the Joint Science and Technology Projects of Bijie (No. 2025-121 and No. 2025-40), China, the Guizhou Province Science and Technology Plan Project No. ZK [2024] Key Project 078, the Joint Fund of Bijie City and Guizhou University of Engineering Science (Bijie Science and Technology Union Contract [2023] No. 16), China.

References

1 G. Ramkumar, S. Kannan, V. Mohanavel, S. Karthikeyan and A. Titus, The Future of Green Mobility: A Review Exploring Renewable Energy Systems Integration in Electric Vehicles, *Results Eng.*, 2025, **27**, 105647.

2 T. Hai, N. S. S. Singh and F. Jamal, Energy management of a microgrid with integration of renewable energy sources considering energy storage systems with electricity price, *J. Energy Storage*, 2025, **110**, 115191.

3 E. Nivolianiti, Y. L. Karnavas and G. Chatziaslanoglou, Techno-economic and life cycle cost analysis for hybrid short-sea passenger vessels based on optimization of different energy storage configurations and management, *Energy Convers. Manage.*, 2025, **343**, 120148.

4 J. Zhang, S. Ding, Z. Lu, X. Kong, X. Guo and J. Zhang, Towards net-zero: Coupling carbon mineralization with seasonal energy storage in integrated energy systems planning, *Appl. Energy*, 2025, **393**, 126065.

5 D. P. Bhattarai, S. Aryal, P. K. Mishra, T. Shrestha, P. L. Homagai, H. B. Oli, *et al.*, Exploring electrochemical performance of Zanthoxylum armatum seed-derived activated carbon using phosphoric acid (H3PO4) for sustainable energy storage applications, *Carbon Trends*, 2025, **19**, 100467.

6 Q. Dong, J. Wu and J. Lu, Probe the Role of Oxygen Anionic Redox in High-Energy-Density Battery with Advanced Characterization Techniques, *Adv. Energy Mater.*, 2025, **15**(22), 2500282.

7 M. Tariq, K. Ahmed, Z. Khan and M. P. Sk, Biomass-derived carbon dots: sustainable solutions for advanced energy storage applications, *Chem.–Asian J.*, 2025, **20**(9), e202500094.

8 J. Aslam, M. A. Waseem, L. Chen, Y. Xu, W. Sun, Y. Wang, *et al.*, Advancing Green Batteries: The Role of Lignin-Derived Carbon in Alkali Metal Ion Energy Storage, *Batter. Supercaps*, 2025, **8**, 2500108.

9 Y. Anwar, M. Khan, A. Mujtaba, U. Younas, M. Fatima, D. O. Alshahrani, *et al.*, Synergistic enhancement of electrochemical performance in g-C3N4@ SnS2 heterostructures for advanced supercapacitor applications, *Diamond Relat. Mater.*, 2025, **156**, 112390.

10 A. İ. Kömür, Ç. Kızıl and C. Karaman, Nature's blueprint for energy: biomass-derived heteroatom-doped graphene materials for advanced energy applications, *Carbon Lett.*, 2025, **35**, 919–961.

11 K. Shafiei, A. Seifi and M. T. Hagh, A novel multi-objective optimization approach for resilience enhancement considering integrated energy systems with renewable energy, energy storage, energy sharing, and demand-side management, *J. Energy Storage*, 2025, **115**, 115966.

12 H. S. Biswas and A. K. Kundu, Hydrogenated Diamond-Like Carbon (HDLC) as Energy Storage Nanomaterials: A Review, *Energy Storage*, 2025, **7**(4), e70191.

13 M. Rafeeq, S. Ahmad, A. Sami, K. Z. Khan, Z. Haidar, F. Ahmed, *et al.*, Facile hydrothermal fabrication of In2O3/Fe2O3 as potential electrode material for supercapacitor, *Electrochim. Acta*, 2025, **524**, 145963.

14 S. Banerjee, B. Mordina, P. Sinha and K. K. Kar, Recent advancement of supercapacitors: A current era of supercapacitor devices through the development of electrical double layer, pseudo and their hybrid supercapacitor electrodes, *J. Energy Storage*, 2025, **108**, 115075.

15 R. K. Maurya, A. Agarwal, R. Gupta, S. M. Islam and R. Sharma, Recent technological advancement in asymmetric supercapacitors: A comprehensive review, *J. Power Sources*, 2025, **640**, 236818.

16 C. V. M. Gopi, S. Alzahmi, V. Narayanaswamy, R. Vinodh, B. Issa and I. M. Obaidat, Supercapacitors: A promising solution for sustainable energy storage and diverse applications, *J. Energy Storage*, 2025, **114**, 115729.

17 M. Islam, M. S. Hossain, B. Adak, M. M. Rahman, K. kubra Moni, A. S. Nur, *et al.*, Recent advancements in carbon-based composite materials as electrodes for high-performance supercapacitors, *J. Energy Storage*, 2025, **107**, 114838.

18 J. Cheng, B. Mi, Q. Wang, H. Wang, T. Zhou, Y. Li, *et al.*, Research on magnetron sputtering thin films as electrode materials for supercapacitors, *Chem. Eng. J.*, 2025, **509**, 161242.

19 N. Singh, V. Singh, N. Bisht, P. Negi, A. Dhyani, R. K. Sharma, *et al.*, A comprehensive review on supercapacitors: Basics to recent advancements, *J. Energy Storage*, 2025, **121**, 116498.

20 M. M. Khan, S. Ahmad, S. I. A. Shah, A. Shan, A. Junaid, J. Zahid, *et al.*, Harnessing perovskite strontium cobalt oxide anchored on scheelite BiVO4 for effective electrochemical water splitting, *Int. J. Hydrogen Energy*, 2025, **196**, 152599.

21 C. Jing, S. Tao, B. Fu, L. Yao, F. Ling, X. Hu, *et al.*, Layered double hydroxide-based nanomaterials for supercapacitors and batteries: Strategies and mechanisms, *Prog. Mater. Sci.*, 2025, **150**, 101410.

22 P. Chaluvachar, Y. Sudhakar, G. Mahesha, V. G. Nair, N. Desai and D. K. Pai, Emerging role of graphitic carbon nitride in advanced supercapacitors: a comprehensive review, *J. Energy Chem.*, 2025, **103**, 498–524.

23 D. Cevher and A. Cirpan, Design, strategies and recent advances in conjugated polymers for supercapacitors, *J. Energy Storage*, 2025, **109**, 115246.
24 S. Abdus, S. Ahmad, S. Ai-Dang, Z. Sijie, F. Liming, F. Saima, *et al.*, Engineered Cu0. 5Ni0. 5Al2O4/GCN Spinel Nanostructures for Dual-Functional Energy Storage and Electrocatalytic Water Splitting, *Processes*, 2025, **13**(7), 2200.
25 Y. Xie, C. G. Nuñez, H. Wang, X. Gao, H. Zhang, F. Jiang, *et al.*, Hollow transition metal chalcogenides derived from vanadium-based metal organic framework for hybrid supercapacitors with excellent energy-density and stability, *J. Colloid Interface Sci.*, 2025, **680**, 446–455.
26 S. Sherin, R. Rai, M. S. Yadav and A. L. Sharma, Investigating the Electronic Properties and Quantum Capacitance of Transition Metal Sulfides MS2 (M= Ti, Mo, W, V, Nb, Ta, Fe, Cu, Co): A DFT Study for High-Performance Supercapacitors, *Mater. Chem. Phys.*, 2025, **345**, 131251.
27 S. C. Caroline, S. V. Badrinarayanan, S. Buvaneswaran, S. Ghosh and S. K. Batabyal, 2D Van der Waal heterostructured bitransition mixed chalcogenide engineered NixCo1-xSSe-based supercapacitors with extended calendar life, *J. Energy Storage*, 2025, **122**, 116597.
28 D. Muhammad, X. Liu, H. Hou, X. Yu, J. Rong and J. Riaz, Noval synthesis of systematized FeS/CuO nanostructure efficacious electrode material for escalating asymmetric supercapacitors, *J. Alloys Compd.*, 2025, **1016**, 178877.
29 P. Naveenkumar, M. Maniyazagan, N. Kang, H.-W. Yang and S.-J. Kim, MoF-derived CuCo2S4@ FeS2 nanohybrids for supercapacitor applications, *Electrochim. Acta*, 2025, **513**, 145546.
30 Q. Van Nguyen, Q. Van Truong, P. Q. Le and H. T. Bui, Facile Synthesis of FeS/C Composites as Electrode Material for Electrochemical Supercapacitors, *J. Mater. Eng. Perform.*, 2025, **34**, 25538–25544.
31 M. Iqbal, A. Singh, M. Alam, A. Arya and S. K. Mahapatra, Core–shell mesoporous carbon@ FeS 2 nanocubes for advanced quasi-solid-state symmetric and asymmetric configurations, *New J. Chem.*, 2025, **49**, 12331–12338.
32 S. Ali, A. Shakoor, M. Raza and A. Ahmad, Facile synthesis of zinc cobalt sulfide and composite with graphitic carbon nitride (ZCS@ GCN) for photocatalysis and electrode for energy storage applications, *Mater. Chem. Phys.*, 2025, **334**, 130431.
33 G. R. Reddy, M. A. Ghanem, S. W. Joo and M. Kang, Redox-active Ni-doped g-C_3N_4-$Cu_3V_4S_8$ nanocomposite for battery-type hybrid supercapacitors, *Chem. Eng. J.*, 2025, **517**, 164418.
34 M. Vaishali, N. Priyadarshini, I. Perumal and K. K. Tadi, Construction of manganese molybdates integrated nanosheet like graphitic carbon nitride as electrode material for symmetric and asymmetric supercapacitors, *J. Energy Storage*, 2025, **117**, 116156.
35 M. Hussain, S. D. Alahmari, F. Alharbi, S. R. Ejaz, M. Abdullah, S. Aman, *et al.*, Hydrothermal synthesis of the NiS@ g-C3N4 nanohybrid electrode material for supercapacitor applications, *J. Energy Storage*, 2024, **80**, 110289.
36 T. Kulandaivel, M. Gopalakrishnan, W. Limphirat, C. Pornrungroj, W.-R. Liu, A. A. Mohamad, *et al.*, Hybrid g-C3N4/sulfur-enclosed MnS micro/nanorods accelerate electron-ion transport and asymmetric supercapacitor performance, *J. Alloys Compd.*, 2025, **1010**, 178268.
37 S. Maruthasalamoorthy, K. Aishwarya, R. Thenmozhi, R. Nirmala, C. Nagarajan and R. Navamathavan, Superior cyclic stability and electrochemical performance of La supported Bi2S3@ g-C3N4//rGO heterostructure composite for asymmetric supercapacitor devices, *J. Alloys Compd.*, 2023, **967**, 171696.
38 N. Bano, S. I. A. Shah, A. Sami, M. Ali, R. A. Alshgari, S. Mohammad, *et al.*, Development of binder–free Ni3S2/CoS2 nano–composite as electrode material for energy storage application, *Ceram. Int.*, 2024, **50**(23), 49880–49888.
39 A. Sami, M. M. Khan, Z. Haidar, A. A. A. Bahajjaj, S. Riaz, S. Naseem, *et al.*, Enhanced supercapacitor performance of rGO-Supported BaVO3 nanostructures as advanced electrode materials, *Ceram. Int.*, 2024, **51**(7), 8480–8491.
40 S. Manzoor, T. Munawar, S. Gouadria, M. Sadaqat, A. G. Abid, A. Munawar, *et al.*, Nanopetals shaped CuNi alloy with defects abundant active surface for efficient electrocatalytic oxygen evolution reaction and high performance supercapacitor applications, *J. Energy Storage*, 2022, **55**, 105488.
41 H. Khani and O. Moradi, Influence of surface oxidation on the morphological and crystallographic structure of multi-walled carbon nanotubes via different oxidants, *J. Nanostruct. Chem.*, 2013, **3**, 73.
42 J. J. Vijaya, G. Sekaran and M. Bououdina, Effect of Cu2+ doping on structural, morphological, optical and magnetic properties of MnFe2O4 particles/sheets/flakes-like nanostructures, *Ceram. Int.*, 2015, **41**(1), 15–26.
43 F. Noreen, A. Junaid, A. Nazir, S. Arshad, K. Bibi, A. Batool, *et al.*, An effective bi-functional electrocatalyst for electrochemical water splitting using NiCo2O4 nanoparticles decorated with Polypyrrole nanocomposite, *Fuel*, 2025, **397**, 135381.
44 T. Ilayas, S. Anjum, M. Y. A. Raja, R. Khurram, M. Sattar and A. Mansoor, Rietveld refinement, 3D view and electrochemical properties of rare earth lanthanum doped nickel ferrite to fabricate high performance electrodes for supercapacitor applications, *Ceram. Int.*, 2023, **49**(17), 28864–28877.
45 İ. Uzun, Methods of determining the degree of crystallinity of polymers with X-ray diffraction: a review, *J. Polym. Res.*, 2023, **30**(10), 394.
46 M. Wang, X. Shi, Z. Wen, Y. Gu, Q. Feng, K. Ma, *et al.*, A crystallinity control strategy for controllable Heterogeneous-Homogeneous reaction and catalytic performance in wet-mechanochemical synthesized FeS2 Fenton system, *Sep. Purif. Technol.*, 2025, **355**, 129683.
47 D. R. Telange, A. T. Patil, A. M. Pethe, A. A. Tatode, S. Anand and V. S. Dave, Kaempferol-phospholipid complex: formulation, and evaluation of improved solubility, in vivo bioavailability, and antioxidant potential of kaempferol, *J. Excipients Food Chem.*, 2016, **7**(4), 89.

48 G. Xiong, H. Xu, J.-Z. Cui, Q.-L. Wang and B. Zhao, The multiple core–shell structure in Cu 24 Ln 6 cluster with magnetocaloric effect and slow magnetization relaxation, *Dalton Trans.*, 2014, **43**(15), 5639–5642.
49 S. Albert, S. Bauerecker, E. S. Bekhtereva, I. B. Bolotova, H. Hollenstein, M. Quack, *et al.*, High resolution FTIR spectroscopy of fluoroform 12CHF3 and critical analysis of the infrared spectrum from 25 to 1500 cm− 1, *Mol. Phys.*, 2018, **116**(9), 1091–1107.
50 Q. Shen, C. Wu, Z. You, F. Huang, J. Sheng, F. Zhang, *et al.*, g-C3N4 nanoparticle@ porous g-C3N4 composite photocatalytic materials with significantly enhanced photo-generated carrier separation efficiency, *J. Mater. Res.*, 2020, **35**(16), 2148–2157.
51 A. Matamoros-Veloza, O. Cespedes, B. R. Johnson, T. M. Stawski, U. Terranova, N. H. de Leeuw, *et al.*, A highly reactive precursor in the iron sulfide system, *Nat. Commun.*, 2018, **9**(1), 3125.
52 Z. Wang, C. Liu, G. Shi, G. Wang, H. Zhang, Q. Zhang, *et al.*, Preparation and electrochemical properties of electrospun FeS/carbon nanofiber composites, *Ionics*, 2020, **26**(6), 3051–3060.
53 M. F. Iqbal, M. N. Ashiq and M. Zhang, Design of metals sulfides with carbon materials for supercapacitor applications: a review, *Energy Technol.*, 2021, **9**(4), 2000987.
54 X. Zhu, Recent advances of transition metal oxides and chalcogenides in pseudo-capacitors and hybrid capacitors: A review of structures, synthetic strategies, and mechanism studies, *J. Energy Storage*, 2022, **49**, 104148.
55 G. Nabi, K. N. Riaz, M. Nazir, W. Raza, M. B. Tahir, M. Rafique, *et al.*, Cogent synergic effect of TiS2/g-C3N4 composite with enhanced electrochemical performance for supercapacitor, *Ceram. Int.*, 2020, **46**(17), 27601–27607.
56 S. Vinoth, K. Subramani, W.-J. Ong, M. Sathish and A. Pandikumar, CoS2 engulfed ultra-thin S-doped g-C3N4 and its enhanced electrochemical performance in hybrid asymmetric supercapacitor, *J. Colloid Interface Sci.*, 2021, **584**, 204–215.
57 K. Subhash, M. Benoy, J. Duraimurugan, S. Prabhu, R. Siranjeevi, R. Ramesh, *et al.*, Synergistic effect of NiS/g-C3N4 nanocomposite for high-performance asymmetric supercapacitors, *Inorg. Chem. Commun.*, 2022, **142**, 109719.
58 M. Karuppaiah, X. Benadict Joseph, S.-F. Wang, B. Sriram, G. Antilen Jacob and G. Ravi, Engineering architecture of 3D-urchin-like structure and 2d-nanosheets of Bi2S3@ g-C3N4 as the electrode material for a solid-state symmetric supercapacitor, *Energy Fuels*, 2021, **35**(15), 12569–12580.
59 C. Zhao, X. Shao, Z. Zhu, C. Zhao and X. Qian, One-pot hydrothermal synthesis of RGO/FeS composite on Fe foil for high performance supercapacitors, *Electrochim. Acta*, 2017, **246**, 497–506.
60 S. Venkateshalu, P. G. Kumar, P. Kollu, S. K. Jeong and A. N. Grace, Solvothermal synthesis and electrochemical properties of phase pure pyrite FeS2 for supercapacitor applications, *Electrochim. Acta*, 2018, **290**, 378–389.
61 D. Muhammad, S. H. Shah, S. Elaissi, N. Ali, M. M. Al-Hinaai and S. Ahmad, Facile synthesis of FeS@ MoS2 nanocomposite material: an advantageous electrode for high-performance supercapacitor, *Ionics*, 2025, **31**, 6131–6144.
62 M. S. Javed, T. Najam, M. Sajjad, S. S. A. Shah, I. Hussain, M. Idrees, *et al.*, Design and fabrication of highly porous 2D bimetallic sulfide ZnS/FeS composite nanosheets as an advanced negative electrode material for supercapacitors, *Energy Fuels*, 2021, **35**(18), 15185–15191.
63 L. G. Ghanem, M. A. Hamza, M. M. Taha and N. K. Allam, Symmetric supercapacitor devices based on pristine g-C3N4 mesoporous nanosheets with exceptional stability and wide operating voltage window, *J. Energy Storage*, 2022, **52**, 104850.
64 S. A. Ansari and M. H. Cho, Simple and large scale construction of MoS2-g-C3N4 heterostructures using mechanochemistry for high performance electrochemical supercapacitor and visible light photocatalytic applications, *Sci. Rep.*, 2017, **7**(1), 43055.
65 Y. Xu, Y. Zhou, J. Guo, S. Zhang and Y. Lu, Preparation of SnS2/g-C3N4 composite as the electrode material for Supercapacitor, *J. Alloys Compd.*, 2019, **806**, 343–349.